journal
J. Am. Ceram. Soc., 79 [5] 1201-12 (1996)

Microstructural Evolution during the Sintering of Nanostructured Ceramic Oxides

Andrew J. Allen,[*,†,‡] Susan Krueger,[†] Ganesh Skandan,[§] Gabrielle G. Long,[*,†] Horst Hahn,[§,¶] Helen M. Kerch,[*,†,††] John C. Parker,[*,‡‡] and Mohammad N. Ali[‡‡]

[†]Materials Science and Engineering Laboratory, National Institute of Standards and Technology, Gaithersburg, Maryland 20899

[‡]Department of Materials and Nuclear Engineering, University of Maryland, College Park, Maryland 20742

[§]Department of Mechanics and Materials Science, Rutgers University, Piscataway, New Jersey 08855

[¶]Department of Materials Science, Technische Hochschule Darmstadt, 64295 Darmstadt, Germany

[††]Office of Basic Energy Sciences, U.S. Department of Energy, Germantown, Maryland 20545

[‡‡]Nanophase Technologies Corporation, Burr Ridge, Illinois 60521

Using small-angle scattering, together with density measurements, X-ray diffraction, nitrogen adsorption, and both transmission and scanning electron microscopy, the microstructural evolution during sintering in nanostructured ceramic oxides has been studied. The availability of samples with sufficient size and uniformity has permitted absolute calibration of the scattering data and made possible determinations of microstructural parameters and surface areas that are statistically representative of the undisturbed nanophase morphologies. A fully quantitative microstructural model has been developed, and the effects of varying processing parameters during powder synthesis and sintering have been assessed. Predictions are made regarding the achievable sintered full-density microstructures.

I. Introduction

The potential of nanophase or nanostructured ceramics, both as intermediate-stage products (offering superior formability prior to final heat treatment) and as final-component products (offering enhanced mechanical properties for intermediate temperature applications) depends on gaining a better understanding and control of the microstructural evolution during processing. This is because of the tendency for the grains to coarsen during sintering. Thus, while suitably uniform nanophase powder materials are becoming increasingly available, challenges remain in the fabrication of fully dense nanostructured products.[1,2] Some of these challenges result from agglomeration and aggregation of the nanosized grains during powder synthesis. A promising method for avoiding agglomeration of the powder is the inert gas condensation (IGC) powder synthesis technique.[3] However, there remains a need to understand better the effects of varying the processing parameters on the subsequent evolution of the nanophase structure during consolidation and sintering. In this connection, the pore and grain size distributions, as well as the grain/pore interfacial surface areas, need to be characterized as a function of sintered density for a range of synthesis and sintering conditions. The effects of phase transformations, and of pressure-, vacuum-, and air-sintering are also of relevance to an increased understanding of the resulting densified microstructures.

A predictive knowledge of nanophase microstructural development ultimately depends on obtaining quantitative statistically significant information that is representative of the microstructures present. Such information contrasts with, and complements, the detailed qualitative data supplied by electron microscopy, which is localized over a few grains. Small-angle scattering (SAS) is one technique which can give a nondestructive statistical account of the representative microstructures. However, until recently it has been difficult to obtain absolute calibrations of the scattering data, due to problems associated with producing uniform samples of a suitable size and shape, as has been discussed elsewhere.[4]

The purpose of this paper is to describe studies of the microstructural evolution during the sintering of IGC-produced nanophase ceramic oxides. Ceramic oxides are of particular interest, because the sintered microstructures are less likely than those of other nanostructured systems to be affected by oxygen contaminants on the grain boundaries.[5,6] The studies described in this paper are based on small-angle neutron scattering (SANS) and ultrasmall-angle X-ray scattering (USAXS), complemented by X-ray diffraction (XRD), scanning and transmission electron microscopy (SEM and TEM), density measurements, and analyses of nitrogen adsorption and desorption isotherms using the Brunauer–Emmett–Teller equations (BET).

Two ceramic systems are discussed: nanostructured yttria (n-Y_2O_3) (prepared in the Department of Mechanics and Materials Science, Rutgers University, Piscataway, NJ, from nanophase powder supplied by Nanophase Technologies Corporation, Burr Ridge, IL) and nanostructured zirconia (n-ZrO_2) (prepared at Rutgers University from nanophase powder made at Rutgers). For simplicity, two pure materials have been studied, but n-Y_2O_3 and n-ZrO_2 have been chosen because of the technological potential of nanostructured yttria-stabilized zirconia (YTZP) in ceramic processing. In the sections that follow, the microstructural changes during sintering in n-Y_2O_3 and n-ZrO_2 are followed and compared. It is shown how absolute calibration of the data reveals small-angle scattering to be dominated by the grain/pore interface scattering. By applying a suitable model, the microstructural evolution of n-ZrO_2 during sintering has been quantitatively characterized, and the results for some key microstructural parameters are presented. Finally, in our concluding remarks, we show how these parameters can be combined to predict the fully dense microstructures.

M. P. Harmer—contributing editor

Manuscript No. 192648. Received May 2, 1995; approved November 15, 1995.
Supported in part by the National Science Foundation under Agreement No. DMR-9122444.

[*]Member, American Ceramic Society.

[†]National Institute of Standards and Technology.

[‡]University of Maryland.

[§]Rutgers University.

[¶]Technische Hochschule Darmstadt.

[††]U.S. Department of Energy.

[‡‡]Nanophase Technologies.

II. Experimental Discussion

(1) Nanostructured Materials Studied

Both the n-Y_2O_3 and n-ZrO_2 studied were prepared from powders produced using the IGC process.[3] For the n-Y_2O_3, precursor yttrium metal was evaporated from a resistively heated tungsten crucible in a low-pressure helium atmosphere of 1.3 kPa ($\approx$10 torr). The chamber had been previously degassed by heating the crucible and the walls of the chamber, while evacuating it by a turbomolecular pump. When a suitable vacuum had been attained, $\approx$1.5 μPa (1.1×10^{-8} torr), the chamber was back-filled with ultrahigh purity helium to the required pressure, and the crucible was slowly heated to evaporate the yttrium. Condensate from the convecting yttrium precursor vapors was collected as nanoparticles on a liquid-nitrogen-filled rotating cold finger, placed $\approx$200 mm away from the crucible. Once evaporation was complete, the helium was removed and pure oxygen was introduced into the chamber at a controlled rate, which was found to be critical in preventing agglomeration of the particles in the resulting oxidizing exothermic reaction. The yttrium nanoparticles were converted into n-Y_2O_3 powder particles of mean diameter $\approx$8 nm (as determined by XRD and both SEM and TEM). The n-Y_2O_3 powder was consolidated (at Rutgers) into 0.5–2.0 mm thick pellets with a consolidation pressure of 500 MPa at room temperature (as-pressed samples) and at 550°C for 3 h (hot-pressed samples). The particle sizes and the pressed-sample densities (56% theoretical density (TD)) depended principally on the rate of evaporation from the tungsten crucible and on the gas pressures and temperatures. The as-pressed samples were sintered in air for 5 h at 600°, 900°, and 1200°C for this study, giving sintered densities of 71% TD, 85% TD, and nearly 100% TD, respectively. As for all the nanophase samples, these bulk densities were measured using Archimedes' principle applied to immersion in water. The samples were coated with a thin layer of grease (weighing less than 0.4% of the sample weight) to prevent errors resulting from water ingression into the pores. In most cases, the bulk density could also be measured from the geometry and weight of the samples, and consistent results were obtained.

The principal difference in the fabrication of the n-ZrO_2 powder at Rutgers University was in the use of ZrO as the precursor in place of yttrium metal. The helium gas pressure during evaporation was 0.27 kPa ($\approx$2 torr), giving a slow evaporation rate of $\approx$8.6 $\mu g \cdot s^{-1}$ (0.5 $g \cdot min^{-1}$). Following oxidation, consolidation of the resulting nanoparticles, of diameter $\approx$6 nm (as determined by TEM), was carried out at a uniaxial pressure of 400 MPa, resulting in 0.5 mm thick pellets of 46.3% TD. These samples were sintered in air for 5, 10, 20, and 40 min at 800°C, and sintered under a 670 μPa ($\approx 5 \times 10^{-6}$ torr) vacuum for 2.5, 5, 10, 20, and 40 min at both 800° and 850°C. An additional n-ZrO_2 sample was prepared to detect microstructural changes introduced by post-vacuum-sinter annealing at the sintering temperature in air, a procedure used to restore stoichiometry following vacuum sintering. This sample was annealed in air at 800°C for 2 h, after cooling under vacuum from the 800°C sintering temperature (having been sintered for 20 min). Densities for all the n-ZrO_2 samples are discussed below.

(2) Microstructural Characterization Using Small-Angle Scattering and XRD

The principles of small-angle scattering are discussed in detail elsewhere.[7] Figure 1 shows the geometry of a typical SANS experiment. In the present experiments, carried out using the NIST/Exxon/University of Minnesota/Texaco 30 m SANS instrument at the Cold Neutron Research Facility (CNRF), National Institute of Standards and Technology, Gaithersburg, MD, a collimated beam of neutrons, of wavelength, λ, 0.55 nm for n-Y_2O_3, 1.0 nm for n-ZrO_2, and $\Delta\lambda/\lambda$ resolution 15%, was passed through a parallel-sided sample of $\approx$0.5 mm thickness and 3–8 mm diameter. A small component of the incident beam was scattered out of the straight-through beam direction by inhomogeneities in the sample microstructure, and the scattered component was registered on the instrument's two-dimensional detector array. With no preferred orientation in the sample microstructure, the scattering was circularly symmetric about the incident beam direction. The SANS data were corrected for empty beam and background counts, calibrated against a scattering standard, and radially summed. By changing the instrument configuration, data were obtained over a range of the scattering wavevector, Q ($Q = (4\pi/\lambda) \sin \theta$, where 2θ is the angle of scatter), of 0.03–1.4 nm^{-1} for n-Y_2O_3. For n-ZrO_2, further experiments using the NIST/NSF 30 m SANS, also at the CNRF, extended the Q range, giving 0.025–5.0 nm^{-1}. Using appropriate analysis of the radially summed, absolute-calibrated SANS data, this Q range was found to be sufficient to determine the volume fraction size distribution of scattering features of up to $\approx$100 nm diameter, associated with the scattering at smaller Q values. The lower size limit was determined by the level of incoherent background scattering, rather than by the maximum Q value attained, and was found to be 1–2 nm.

For the sintering study of n-Y_2O_3, Fig. 2(a) shows radially summed, approximately calibrated small-angle scattering cross-section, $d\Sigma/d\Omega$, data as a function of Q. ($d\Sigma/d\Omega$ is the probability rate, per unit incident neutron flux and per unit sample volume, of scattering into unit solid angle, Ω, about any one direction defined by a given scattering angle, 2θ, or magnitude of the scattering wavevector, Q.) These data show many of the hallmarks of SANS from nanostructured materials revealed in previous studies,[8] in particular, the appearance and later disappearance of an interference peak as the sintered density is increased. Coarsening of the grain/pore morphology at high sintering temperatures is also apparent in the shift in the scattering to lower Q for the sample sintered at 1200°C. Figure 2(b) shows absolute $d\Sigma/d\Omega$ data for selected n-ZrO_2 samples, and Fig. 2(c) shows the effects, on the SAS data, of postsinter annealing in air after vacuum-sintering. Figure 2 includes SAS model fits discussed later. Figure 3 shows typical absolute-calibrated scattering cross-section data for n-ZrO_2. The Q range has been extended down to 0.008 nm^{-1} with internormalized USAXS measurements on a specimen, thinned to less than 200 μm thickness. USAXS measurements were performed at the NIST USAXS instrument at the National Synchrotron Light Source, Brookhaven National Laboratory. This is a Bonse–Hart-type instrument,[9] where 0.124 nm wavelength X-rays and crystal optics were used to provide an ultrahigh resolution for small-angle scattering studies.

Figure 3 also indicates how small-angle scattering can be associated generically with the principal features of the microstructural model, presented in detail below to represent the microstructure shown schematically in Fig. 4. It is assumed that the scattering features are oblate pores (oblate diameters, D_O) between the grains, and that the interference effects are associated with the distances, D_{int}, between pores, across the intervening grains. The model is sufficiently flexible to represent a range of nanoscale microstructures. For example, significant agglomeration of the nanoparticles might be characterized by a somewhat larger D_{int} than D_O, even at intermediate porosities. Grain-coarsening during sintering might be indicated by D_O and D_{int} increasing together as the porosity decreases.

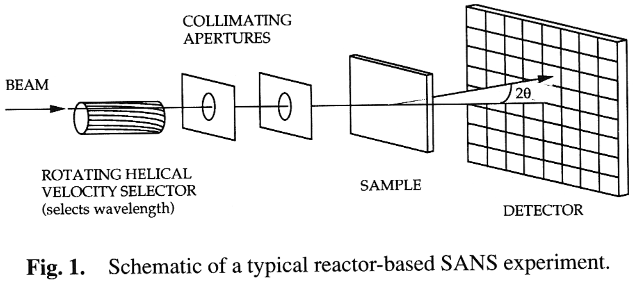

Fig. 1. Schematic of a typical reactor-based SANS experiment.

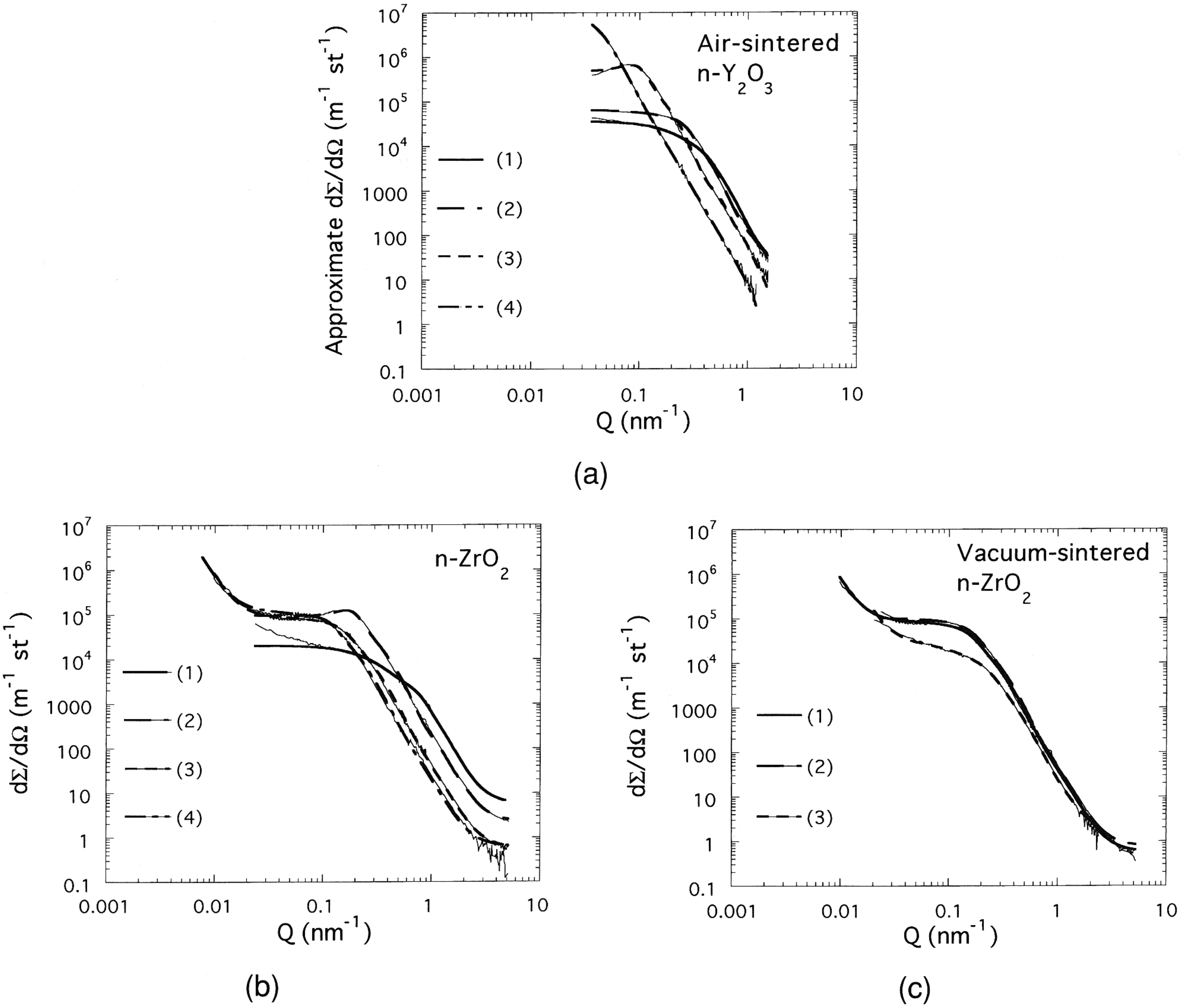

Fig. 2. (a) SANS data and model fits for n-Y_2O_3: (1) as-pressed, and air-sintered for 5 h at (2) 600°C, (3) 900°C, and (4) 1200°C. Thin lines follow the data and thick lines follow the fits. (b) SANS data and model fits for representative n-ZrO_2 samples studied: (1) as-pressed, (2) air-sintered for 20 min at 800°C, (3) vacuum-sintered for 20 min at 800°C, and (4) vacuum-sintered for 20 min at 850°C. For the two vacuum-sintered samples, the data have been extended to lower Q using USAXS. Thin lines follow the data and thick lines follow the fits. (c) SANS data and model fits for n-ZrO_2: (1) vacuum-sintered for 20 min at 800°C without postsinter anneal; (2) as (1) but with postvacuum-sinter anneal in air for 2 h at 800°C; and (3) vacuum-sintered for 60 min at 975°C, discussed later in the text. Thin lines follow the data and thick lines follow the fits.

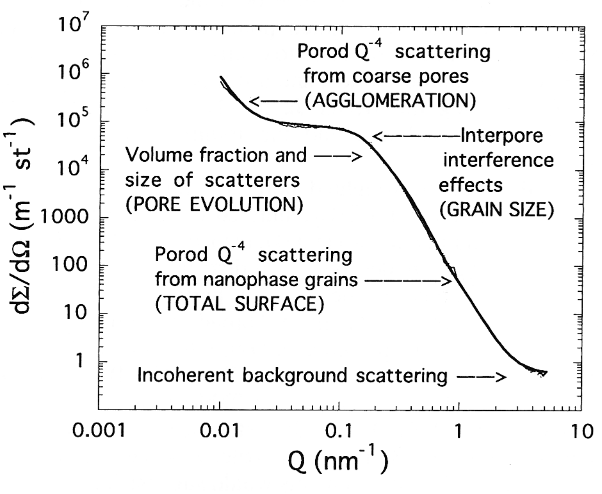

Fig. 3. Schematic showing how SAS data for n-ZrO_2, exhibiting interpore interference effects, can be related generically to the underlying grain/pore microstructure. The thin line follows the data and the thick line follows the fit.

Concerning the SAS data, some basic points can be made prior to modeling. First, the contribution arising from the pore/grain interface dominates the scattering. Other features, such as low-density grain-boundary disordered phases, proposed elsewhere,[10] cannot scatter sufficiently strongly to give the SANS observed, while the pore/grain microstructure easily accounts for all of the scattering. Furthermore, ultrafine microstructural complexes on grain boundaries, or small tetrahedral pores at grain-boundary triple junctions, would perturb the extended Porod scattering regime, but this is not observed in the data.

Second, the Q^{-4} Porod scattering range at higher Q values in the data can be used to determine the total pore/grain interfacial surface area, S_v, using Porod's Law:[7] $d\Sigma/d\Omega = 2\pi|\Delta\rho|^2 S_v/Q^4$. The neutron or X-ray scattering contrast, $|\Delta\rho|^2$, is the square of the difference in the neutron or X-ray scattering-length density, ρ, between that in the scattering pores and that in the solid grains. The scattering lengths themselves are measures of the intrinsic strengths of the neutron or X-ray interactions, respectively, with nuclei or whole atoms in the sample. The measure of S_v can be compared with that deduced from applying the microstructural model.

Third, the characteristics of the SANS data, indicated in Figs. 2 and 3, and the changing shape of the data as sintering progresses to high density, seem quite general for nanostructured ceramic materials, regardless of whether or not a

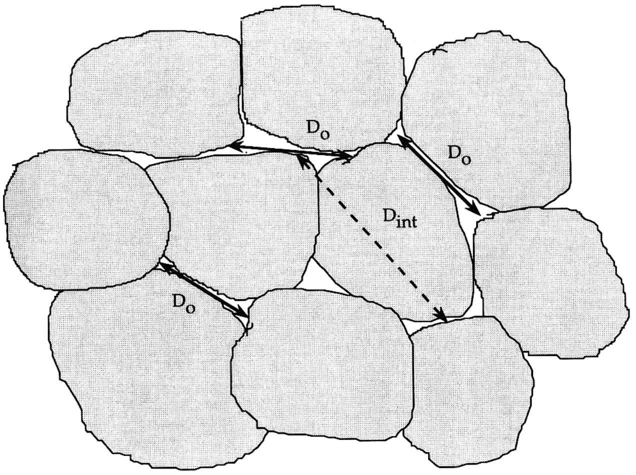

Fig. 4. Schematic of the nanophase grain/pore microstructure. Globular nanophase grains are assumed, with mildly oblate pores between the grains.

metastable phase transformation is involved during sintering. Therefore, a microstructural model, such as that presented here for the sintering of pure n-ZrO_2, should be applicable, in its essential aspects, to sintering studies in a wide range of nanostructured ceramic systems.

For selected n-Y_2O_3 and n-ZrO_2 samples, at various stages of sintering, XRD studies were made to determine both the nanocrystalline phases present and, in some cases, the volume-weighted mean crystallite sizes. The phase determinations were carried out using a rotating-anode X-ray diffractometer and Cu $K\alpha$ radiation. For some samples, grain (crystallite) diameters were also determined from XRD line-broadening measurements and the Scherrer[11] formula. Because, for some samples, the nanocrystalline grains were sufficiently small for the Bragg peaks to become weak and broad, peak overlap was a complicating effect in attempts to distinguish peak-width contributions due to microstrain effects (proportional to the planar spacing, d), from those due to crystallite size (proportional to d^2). Therefore, strain effects were ignored, leading to possible slight underestimates of the grain size determined by XRD. (Note that, in the case of twinned crystallites within a grain, XRD determines overall grain diameters, but, if agglomeration effects are significant, crystallite or subgrain diameters may be measured.)

In n-Y_2O_3, it was found that the nanophase grains remain in the metastable monoclinic phase at low temperatures, but above 800°C, where significant grain growth occurs, this phase transforms to the stable cubic phase.[12] In n-ZrO_2, the original powder was found to be mainly in the metastable tetragonal phase, but a transformation to the stable monoclinic phase occurs on compaction.[13] There is little or no phase transformation during sintering in n-ZrO_2, even at temperatures at which coarsening occurs. It is remarkable that, while the nanophase form of most ceramic materials occurs initially in a metastable phase, possibly due to the Gibbs–Thomson surface-energy effect acting on the small crystallites,[14] there is little evidence that this has an impact on microstructural development during sintering.

The volume-weighted mean crystallite diameters determined from XRD studies were compared with the grain and pore diameters measured by small-angle scattering and other methods, as is shown in Table I. Such detailed comparisons assist in distinguishing grain coarsening, during final-stage sintering, from grain agglomeration, during powder fabrication, consolidation or early-stage sintering.

(3) Microstructural Characterization Using TEM/SEM and BET Studies

TEM and SEM studies were caried out to determine the detailed localized grain/pore morphologies in the nanophase samples and, from these, to establish and confirm the validity of the microstructural model for the interpretation of the small-angle scattering. In selected cases, electron microscopy was also subsequently used to determine the number-weighted median grain diameters. These were compared with the values for the pore and grain sizes, inferred from the microstructural model interpretation of the small-angle scattering data.

A typical bright-field TEM image of the as-synthesized n-ZrO_2 powder, used to fabricate all the n-ZrO_2 samples in the studies presented here, is shown in Fig. 5(a). Some apparent aggregation of the particles into chains was attributable to their extraction from a methanol suspension pretreatment. True aggregation or agglomeration of the powder particles would have resulted in their failure to sustain a stable suspension. For the sintered n-ZrO_2 samples themselves, fracture surfaces were studied by field emission SEM. Since the sample image contrast was poor, the fracture surfaces had to be coated with a thin Au-Cr layer. Figure 5(b) shows a typical SEM image obtained for n-ZrO_2, sintered in air for 20 min at 800°C. Some evidence of grain pullout is apparent, but the morphology is broadly consistent with that presented in Fig. 4.

For the as-synthesized powder, a number-weighted particle size distribution was determined by counting the number of individual particles in the TEM images with mean diameters within different size ranges. The resulting histogram is shown in Fig. 5(c). The distribution is single-moded and approximately lognormal in functional form, with median diameter $\approx$6 nm. For n-ZrO_2, sintered in air for 20 min at 800°C, the SEM studies of fracture surfaces gave the grain size distribution shown in Fig. 5(d). Apart from the presence of a few larger features, this is also approximately lognormal in shape. An estimated number-weighted median grain diameter of $\approx$20 nm is indicated.

These TEM particle and SEM grain diameters are acceptably close to the crystallite sizes determined from XRD, as shown in Table I (particularly when different weightings and averages over the size distributions are considered). This, together with the general appearance of nonagglomerated particles in Fig. 5(b), and the fact that SEM images for n-ZrO_2, vacuum-sintered to much higher densities (see Table I), have a qualitatively similar appearance,[15] suggest not only that the nanoparticles are not significantly agglomerated in the as-synthesized powder, but also that the partially sintered grains do not agglomerate significantly during sintering. In the absence of agglomeration or uneven sintering, it is to be expected that the pore size distributions will mimic the particle size distributions as sintering progresses, although some deviations must occur as full density is approached.

Nitrogen desorption BET measurements[16] were carried out on selected samples to determine both the pore/grain surface areas and the volume-weighted pore size distributions. The isotherms generated were found to exhibit the class IV behavior typical of mesoporous solids, and a full pore size analysis was carried out using the Berrer–Jaynes–Halinda method.[16] The pore diameter resolution and the minimum pore diameter probed were both $\approx$2 nm.

The BET volume-weighted pore size distributions for the as-pressed n-ZrO_2 and n-ZrO_2, sintered in air at 800°C for 20 min, are shown in Figs. 5(e) and (f), respectively. The relatively narrow and single-moded pore size distributions observed are again an indication of the lack of particle agglomeration. Agglomeration would have given a broad or bimodal pore size distribution due to the presence of both intra- and interagglomerate pores.[17] For the as-pressed n-ZrO_2, the BET volume-weighted pore diameter, shown in Table I, is in agreement with the TEM and XRD grain diameter measurements. For the sintered sample, the BET pore diameter is somewhat less than the XRD and SEM measurements would suggest. Table I shows that a similar situation exists for n-Y_2O_3, when compared with the SANS results discussed below, although there is good agreement with the XRD result. The BET results for the sintered samples are probably affected by the constriction of pore

Table I. Comparison of Grain and Pore Diameters Measured by XRD, TEM/SEM, BET and SANS*

Sample	Density (% TD)	XRD grain diameter (nm)	TEM/SEM grain diameter (nm)	BET pore diameter (nm)	BET grain diameter (nm)	SANS $D_{o\,avg}$ (nm)	SANS D_{int} (nm)
n-ZrO_2							
As-pressed	46.3	4.0 (5)	6.0 (5) (powder)	6 (1)	7.5 (15)	7.85 (6)	7.18 (4)
Air-sintered 20 min at 800°C	71.5	25 (2)	20 (2)	9 (1)		24.54 (7)	31.2 (1)
Vacuum-sintered 10 min at 800°C	91.7	30 (2)				26.9 (1)	37.4 (2)
Vacuum-sintered 40 min at 850°C	94.7	51 (3)	45 (2)			31.9 (3)	47.6 (4)
n-Y_2O_3							
As-pressed	56	8 (1)	8 (1) (powder)	6.5 (10)		17.7 (3)	11.5 (1)
Air-sintered 5 h at 900°C	85	33 (2)		36 (2)		54.8 (2)	57.8 (2)

*XRD: volume-weighted mean grain diameter; TEM/SEM: number-weighted median grain diameter; BET: volume-weighted mean pore diameter, inferred grain diameter; SANS: number-weighted mean oblate pore diameter, $D_{o\,avg}$, interpore interference distance, D_{int}. All sphere-equivalent diameters, except for oblate pore diameter, $D_{o\,avg}$, where aspect ratio, β, of 1/3 assumed. Estimated standard uncertainties, σ, in least significant digits shown in parentheses.

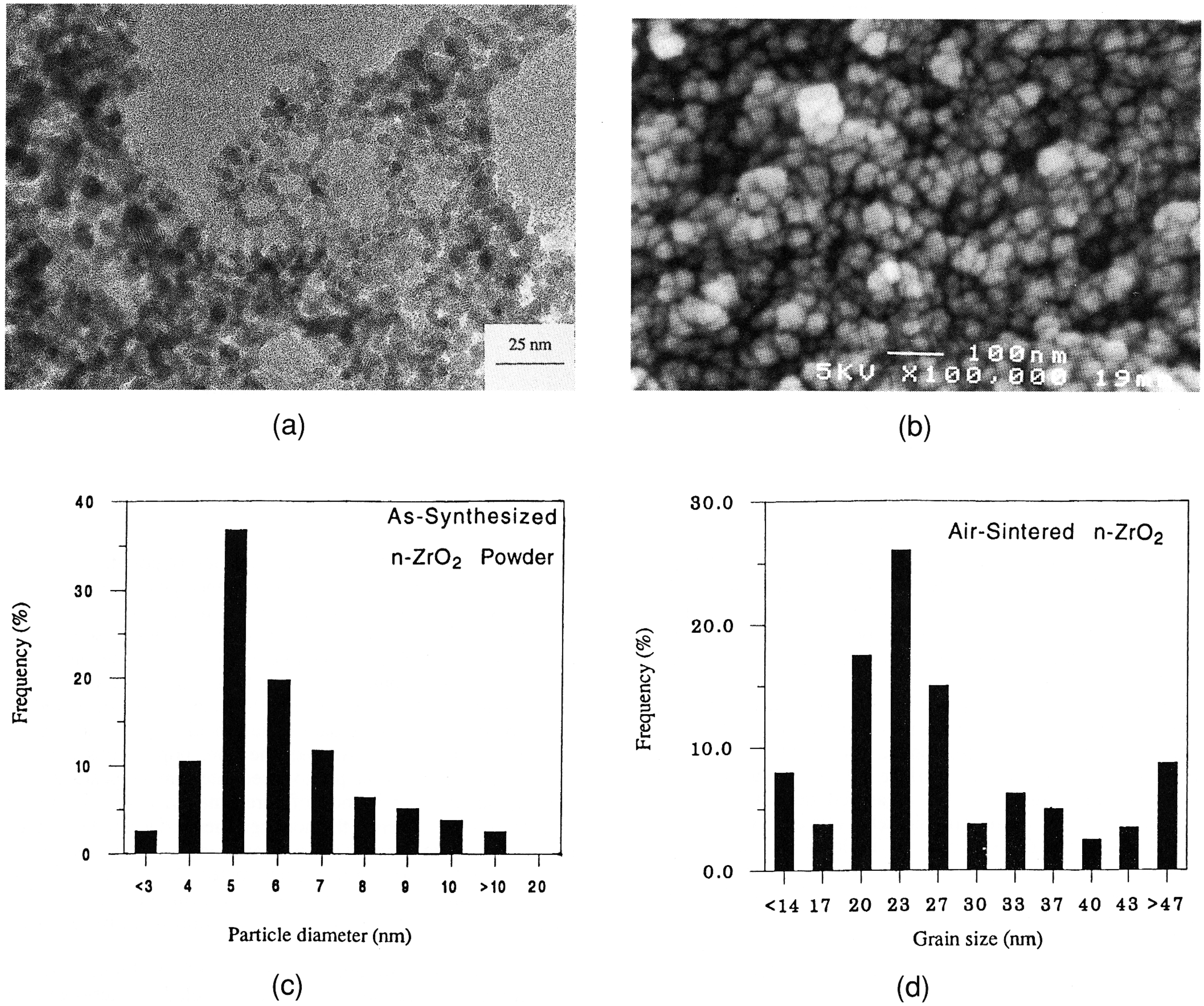

(a) (b)

(c) (d)

Fig. 5. Microstructural characterization of n-ZrO_2 as-synthesized powder, as-pressed or as-compacted green-body sample, and sample air-sintered at 800°C for 20 min: (a) TEM micrograph of as-synthesized powder, (b) SEM micrograph of air-sintered sample. Number-weighted TEM/SEM grain diameter size distributions for (c) as-synthesized powder (TEM), (d) air-sintered sample (SEM). Volume-weighted BET pore diameter size distributions for (e) as-pressed sample, (f) air-sintered sample. SAS model number-weighted oblate pore diameter, D_o, size distributions for (g) as-pressed sample, (h) air-sintered sample.

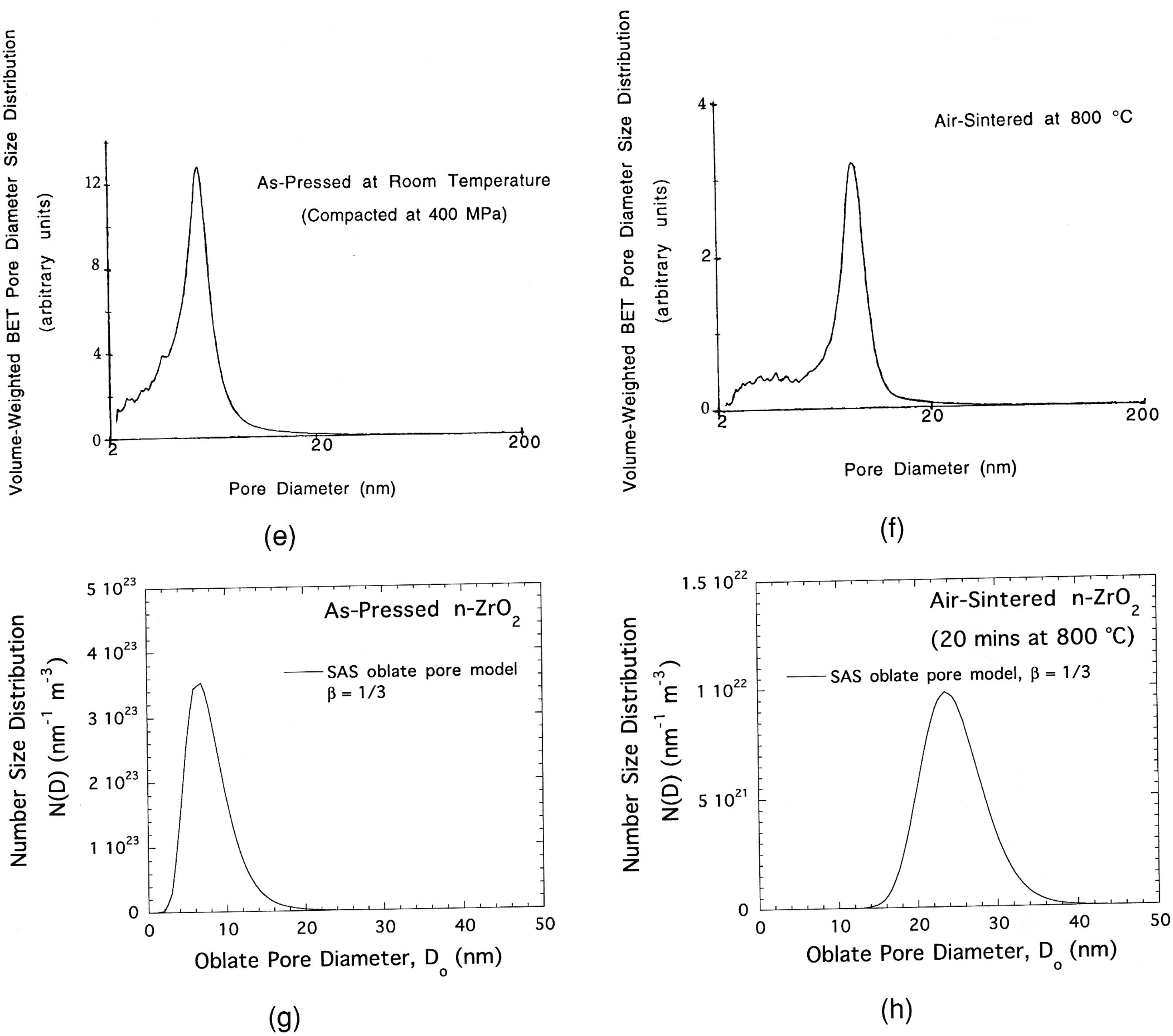

Fig. 5 (Continued).

necks as sintering proceeds. However, like the TEM particle size distribution discussed above, the BET pore size distributions appear lognormal in functional form, even after partial sintering. This supports an assumption of lognormal grain and pore size distributions in the model interpretations of the SANS data.

Single-point BET analysis was also used to determine the specific surface areas of the same n-ZrO_2 samples. These data are presented in Table II, for comparison with those determined from SANS. From the BET surface area and volume-weighted mean pore diameter, and the measured density, an inferred volume-weighted mean grain diameter was back-calculated for the as-pressed n-ZrO_2, shown in Table I. Again, acceptable agreement is obtained. However, the BET surface area for the sintered sample was too low to back-calculate a credible nanophase grain diameter, suggesting that much of the pore/solid surface area was not accessible to nitrogen.

(4) Microstructural Model for Sintering in Nanostructured Ceramics

Figure 4 shows the basic microstructure assumed in the present sintering studies. To model the microstructure mathematically, an idealized model was used, comprising a number-weighted lognormal size distribution of mildly oblate pores between the nanostructured grains. In the low-density as-pressed material, the pores are sufficiently polydispersed, in both size and shape, so that no interference peak in the scattering is discernible. However, for higher intermediate densities, resulting from partial sintering, the pores become discrete. For the n-Y_2O_3 and n-ZrO_2 studied here, these high concentrations of fine pores, distributed throughout the microstructures, were assumed to give the interpore interference effects, observed as peaks or shoulders in the data at intermediate Q. For the more fully sintered densities studied, the pore populations become sufficiently dilute for the pronounced interference peaks to disappear, but the persistence of, presumably, a few localized clusters of pores, even in the nonagglomerated grain morphologies studied here, was found to provide enough interpore interference effects to determine the parameter, D_{int}, shown in Fig. 4. (However, interference scattering effects cannot persist to 100% TD. At some point, the pore concentration must become too dilute.)

Previous models for the interpretation of interference effects in small-angle scattering data either modeled a functional size distribution of interacting spherical scatterers[18–20] or assumed the scatterers to be monodispersed spheroids in both size and shape with a preset aspect ratio.[20,21] The present model was developed from the latter to fit a lognormal size distribution of spheroids with a preset aspect ratio, β, selected from nine

Table II. Comparison of n-ZrO_2 Pore/Grain Surface Areas Measured by BET and SANS*

Sample, n-ZrO_2	Density (% TD)	BET specific surface area (10^3 $m^2 \cdot kg^{-1}$)	SANS population surface, S_{pop} (10^6 $m^2 \cdot m^{-3}$)	SANS Porod surface, S_v (10^6 $m^2 \cdot m^{-3}$)	SANS population specific surface, $S_{g\ pop}$ (10^3 $m^2 \cdot kg^{-1}$)	SANS total (Porod) specific surface, S_g (10^3 $m^2 \cdot kg^{-1}$)
As-pressed	46.3	99 (1)	292 (3)	359 (1)	113 (1)	138 (1)
Air-sintered 20 min at 800°C	71.5	13 (1)	118 (1)	128.7 (2)	29 (1)	32 (1)

*S_{pop} and $S_{g\ pop}$ determined analytically from SAS oblate pore model populations, as discussed in the text. Estimated standard uncertainties, σ, in least significant digits shown in parentheses.

available values. The grain size distributions were expected to correlate, at least approximately, with the pore size distributions.

To model the experimentally determined small-angle scattering cross sections in the present case, it was assumed that the nanostructured material contains spheroids with three orthogonal diameters D_o, D_o, and βD_o. The number of pores per unit sample volume, n_o, was assumed to be distributed over a lognormal number size distribution, $n(D_o)$, such that

$$n(D_o) = \frac{n_o}{[2\pi \ln (D_{o\,med}/D_{o\,mode})]^{1/2}} \left(\frac{1}{D_o}\right) \exp\left\{\frac{-[\ln (D_o/D_{o\,med})]^2}{2 \ln (D_{o\,med}/D_{o\,mode})}\right\} \tag{1}$$

where $D_{o\,mode}$ and $D_{o\,med}$ are, respectively, the modal and median values of D_o for the distribution. The number-weighted mean value of D_o, here denoted $D_{o\,avg}$, is given by $D_{o\,avg} = (D_{o\,med})^{3/2}/(D_{o\,mode})^{1/2}$, and can be compared with the grain size values determined by other methods. The volume fraction of pores in the lognormal population, ϕ_{pop}, is given by $\phi_{pop} = (n_o\pi\beta/6)\{(D_{o\,med})^{15/2}/(D_{o\,mode})^{9/2}\}$, and ϕ_{pop} can be compared with the total porosity, ϕ_{total}, determined from density measurements. Note that a lognormal distribution can be analytically defined by specifying three parameters. Here, it has been found convenient to use ϕ_{pop}, $D_{o\,mode}$, and $D_{o\,med}$, which can be directly incorporated into the fits to the experimental data. (Note also that, for a lognormal size distribution, $D_{o\,mode} < D_{o\,med} < D_{o\,avg}$.)

The small-angle scattering cross section was assumed to be given by

$$d\Sigma/d\Omega = n_o P(Q) S_1(Q) + \text{BGD} + P_{add} \tag{2}$$

where $S_1(Q)$ is an effective modified structure factor that incorporates the interpore interference effects, BGD is the flat incoherent background scattering term, and P_{add} is an additional Porod scattering term discussed below. $P(Q)$ is the scattering form-factor, equal to the square of the scattering amplitude, $F(Q)$, for a single spheroidal pore, averaged over all orientations and over the lognormal number size distribution. Thus, $P(Q)$ is given by[22]

$$P(Q) = \langle|F(Q)|^2\rangle = 8\pi^3\beta^2|\Delta\rho|^2 \int_0^\infty \int_0^1 \frac{n(R_o)}{n_o} |G(QR_o,\beta,X)|^2 \, dX \, dR_o \tag{3}$$

where X is an orientational parameter, $R_o = D_o/2$, and $n(R_o)\,dR_o = n(D_o)\,dD_o$. The function $G(QR_o,\beta,X)$ is given[22] by

$$G(QR_o,\beta,X) = R_o^3 \frac{J_{3/2}(QR_o[1 + (\beta^2 - 1)X^2]^{1/2})}{(QR_o[1 + (\beta^2 - 1)X^2]^{1/2})^{3/2}} \tag{4}$$

where $J_{3/2}(x)$ denotes a Bessel function in "x" to order 3/2.

$S_1(Q)$ is given by

$$S_1(Q) = 1 + B(Q)\,[S(Q) - 1] \tag{5}$$

For a monodispersed population of spherically shaped scatterers, $B(Q) = 1$, and $S_1(Q) = S(Q)$. However, in the present case, $B(Q)$ is modified in an attempt to allow some polydispersity in the shape and the size of the individual pores within the morphology and is given by a ratio of different orientational averages of $F(Q)$:

$$B(Q) = \frac{|\langle F(Q)\rangle|^2}{\langle|F(Q)|^2\rangle} \quad \text{where}$$

$$|\langle F(Q)\rangle|^2 = 8\pi^3\beta^2|\Delta\rho|^2 \left| \int_0^\infty \int_0^1 \frac{n(R_o)}{n_o} G(QR_o,\beta,X) \, dX \, dR_o \right|^2 \tag{6}$$

$S(Q)$ is the interference structure factor for an orientationally random distribution of nearest-neighbor scatterers, based on a Percus–Yevick hard-sphere model.[21] It contains two significant parameters: the local volume (packing) fraction, η, of the interfering pores, and the mean distance between pore centroids, D_{int}. A full description of $S(Q)$ is beyond the scope of this paper, but is discussed in detail elsewhere.[20] Although $S(Q)$ strictly applies to an assembly of interacting spherically shaped scatterers, and no exact description of the case of nonspherical objects is available, use of $B(Q)$ in $S_1(Q)$ provides a good working approximation when the distribution of nearest-neighbor scattering-object centroids is approximately spherically symmetric. This approximation should hold particularly well in the present case of oblate spheroidal pores arranged randomly around globular nanophase grains.

For the n-ZrO_2 sintering studies, best fits were generally obtained for mildly oblate aspect ratios, with $\beta = 1/3$ or $1/2$. For convenience, fits presented here all have $\beta = 1/3$. $D_{o\,avg}$ could be deduced from ϕ_{pop}, $D_{o\,mode}$, and $D_{o\,med}$, and compared with the grain and pore diameters obtained by SEM, TEM, XRD, and BET studies. For a narrow lognormal size distribution of pores and grains, $D_{o\,avg}$ should correlate well with the mean grain diameter, D_{grain}, and there should not be large differences between number-weighted and volume-weighted mean diameters. Thus, if pores are arranged around grains, D_{int} should also give a measure of D_{grain}. For selected samples, both $D_{o\,avg}$ and D_{int} are included in Table I. For n-ZrO_2, as-pressed and after air-sintering for 20 min, the fitted model pore population lognormal size distributions are given in Figs. 5(g) and (h), respectively.

The pore/solid surface area per unit sample volume, S_{pop}, of the lognormal pore population could also be deduced analytically from the following relations:

$$S_{pop} = \frac{6\,\phi_{pop}\chi_s}{D_{o\,med}} \left(\frac{D_{o\,mode}}{D_{o\,med}}\right)^{5/2} \tag{7a}$$

where, for oblate spheroidal pores, the geometric factor, χ_s, is given by

$$\chi_s = \frac{1}{2\beta}\left\{1 + \frac{\beta^2}{(1 - \beta^2)^{1/2}} \ln\left[\frac{1 + (1 - \beta^2)^{1/2}}{\beta}\right]\right\} \quad \text{for } \beta \le 1 \tag{7b}$$

For the n-ZrO_2 samples, values of S_{pop} are given in Table III and can be compared with S_v, determined from the Porod scattering. For the two samples where BET surface areas were measured, specific surfaces are given in Table II, for comparison.

A second Porod scattering term, P_{add}, required to fit the rise in $d\Sigma/d\Omega$ at small Q, can be associated with an additional component of the pore/grain surface area, S_{add}. Attributable to a small number of large pores around agglomerated grains or

Table III. SAS Microstructural Model Fit Results for n-ZrO$_2$*

Sample, n-ZrO$_2$	Sintering time (min)	Density (% TD)	ϕ_{total} (%)	ϕ_{pop}† (%)	$D_{o\,mode}$† (nm)	$D_{o\,med}$† (nm)	$D_{o\,avg}$ (nm)	Local η† (fraction)	D_{int}† (nm)	ΔW‡ (%)	S_{pop} (10^6 m^2·m^{-3})	S_v (10^6 m^2·m^{-3})	Pores per grain
As-pressed:		46.3	53.7(5)	27.2(1)	6.50(4)	7.37(4)	7.85(6)	0.196(2)	7.18(4)	36	292(3)	359(1)	0.92
Sintered in air at 800°C	5	69.3	30.7(5)	27.8(1)	22.46(4)	22.86(4)	23.06(6)	0.180(1)	28.1(1)	13	126(1)	138.3(3)	2.06
	10	70.2	29.8(5)	25.5(1)	22.94(6)	23.42(4)	23.68(7)	0.178(2)	28.4(1)	15	112(1)	121.7(2)	1.77
	20	71.5	28.5(5)	28.0(1)	23.66(6)	24.26(4)	24.54(7)	0.194(1)	31.2(1)	16	118(1)	128.7(2)	2.23
	40	72.2	27.8(5)	27.4(1)	25.32(6)	25.80(4)	26.04(7)	0.174(1)	32.2(1)	14	110(1)	119.6(2)	2.04
Sintered under vacuum at 800°C	2.5	90.0	10.0(2)	8.01(5)	19.9(1)	21.3(1)	22.0(1)	0.085(2)	31.2(2)	26	34.6(3)	36.3(1)	0.62
	5	90.5	9.5(2)	6.58(5)	22.8(1)	24.3(1)	25.0(1)	0.092(2)	34.4(2)	25	25.1(3)	26.9(1)	0.47
	10	91.7	8.3(2)	6.19(5)	24.4(1)	26.1(1)	26.9(1)	0.097(3)	37.4(2)	25	22.0(3)	23.8(1)	0.45
	20	91.4	8.6(2)	6.86(5)	24.4(1)	26.0(1)	26.9(1)	0.095(2)	36.6(2)	26	24.3(3)	26.1(1)	0.47
	40	93.5	6.5(2)	6.57(5)	25.6(1)	27.4(1)	28.4(1)	0.097(2)	39.6(2)	26	22.0(3)	23.7(1)	0.47
Postsinter annealed		88.0	12.0(5)	8.27(5)	27.1(2)	28.3(1)	28.9(2)	0.073(2)	33.9(2)	20	28.6(4)	31.0(1)	0.40
Sintered under vacuum at 850°C	2.5	91.4	8.6(2)	6.31(5)	30.1(2)	31.5(1)	32.2(2)	0.099(3)	36.4(2)	21	19.5(2)	21.7(1)	0.26
	5	92.9	7.1(2)	4.52(5)	31.6(2)	33.3(2)	34.1(3)	0.107(4)	43.9(3)	22	13.0(3)	15.2(1)	0.27
	10	93.3	6.7(2)	5.34(5)	29.7(2)	31.6(2)	32.6(3)	0.128(5)	42.3(3)	25	15.7(3)	18.3(1)	0.31
	20	93.9	6.1(2)	4.26(5)	30.7(3)	33.0(2)	34.2(4)	0.126(5)	47.3(2)	27	11.7(2)	14.8(1)	0.29
	40	94.7	5.3(2)	4.22(5)	27.4(2)	30.3(2)	31.9(3)	0.146(6)	47.6(4)	32	11.7(2)	14.4(1)	0.33

*Estimated standard uncertainties, σ, in least significant digits shown in parentheses. †Fitted parameters. Others parameters derived, or measured independently. BGD and S_{add} omitted. ‡ΔW is fractional width of pore size distribution with respect to $D_{o\,mode}$.

larger particles, S_{add} could be determined from the additional Q^{-4} scattering component, just as S_v was extracted from the Porod scattering at high Q.

III. Results and Discussion

(1) *Validation of SAS Model Fit Results*

In summary, Fig. 5 not only confirms the existence of relatively narrow and correlated pore and grain size distributions, but also indicates an approximately lognormal functional form for these distributions, as explicitly assumed for SAS. When allowance is made for the different shape assumptions and size distribution weightings, the values of $D_{o\,avg}$ and D_{int}, given in Table I for selected n-ZrO$_2$ samples, show satisfactory consistency with the volume-weighted mean crystallite diameters from XRD, and the number-weighted median grain diameters from TEM or SEM. The volume-weighted mean pore diameters from BET also show satisfactory agreement for the as-pressed samples, but indicate a smaller size for the partially sintered samples, an effect probably associated with the presence of constricted pore necks. For the two selected n-Y$_2$O$_3$ samples, the SAS pore diameters, $D_{o\,mode}$, $D_{o\,med}$, and $D_{o\,avg}$, are significantly larger than the XRD/TEM/SEM diameters, and this may indicate a greater degree of agglomeration than for n-ZrO$_2$.

For n-ZrO$_2$, Table I shows $D_{o\,avg}$ as closer than D_{int} to the XRD and TEM/SEM values of D_{grain} at lower and intermediate densities, but D_{int} as closer at the highest densities reached. Table III, which reports in detail the SAS model fit results for the sintered n-ZrO$_2$ samples, shows both $D_{o\,avg}$ and D_{int} as varying in a similar way with density. This is not so for n-Y$_2$O$_3$, where Table I and the fit results for the other n-Y$_2$O$_3$ samples, not tabulated here, indicate that $D_{o\,avg}$ is considerably greater than D_{int} over much of the lower density range. This suggests that, here, the particles neck and attach to one another in short chains.

The interpretation of the SANS scattering features as oblate pores yields, not only good model fits to the SANS data, but also values of ϕ_{pop}, determined from these fits, that approach the total porosities, ϕ_{total} (see Table III). The Table II comparisons of S_{pop}, S_v, and their specific surface equivalents, show how the SAS model pore populations also account for most of the surface areas in the samples. However, the BET surface areas for the sintered samples are significantly less than the SANS Porod surfaces, suggesting that a substantial fraction of the porosity has closed during sintering and, therefore, is inaccessible to BET measurement.

For the sintered n-ZrO$_2$ samples, the rise in the scattering at small Q, P_{add}, can be accounted for by a value of $S_{add} \sim 2.5$ m^2·kg^{-1} (0.0025 m^2·g^{-1}), associated with coarse porosity. However, the nanostructured morphology accounts for more than 98% of the sintered sample volume. In the as-pressed n-ZrO$_2$, although an excellent fit is obtained over much of the Q range using any value of the aspect ratio, β, the extra scattering at low Q is ignored. Without USAXS data, there is insufficient weight to properly fit this component, which could represent a coarse porosity of up to 27% of the sample volume, not otherwise accounted for. While the Q range does not extend to sufficiently low Q to permit a full characterization of the coarser microstructure, modelling of this does not seem to affect significantly the fit parameters for the nanostructured morphology, at least in the partially sintered samples. This coarser regime is not discussed further in the present paper, although it is acknowledged that a substantial volume fraction of coarse pores or agglomerated grains, persisting in partially sintered material, could hinder the achievement of a fully dense nanostructured grain morphology.

(2) *Sintering Study of n-ZrO$_2$*

While, for each n-ZrO$_2$ sintering condition, modest increases occur in grain size and density with sintering time, the curves shown in Fig. 2(b) typify the SAS data and microstructural model fits for each series. Sintering is rapid, with the degree of sintering achieved prior to the earliest sintering times studied being far in excess of further sintering at later times. For the two vacuum-sintered samples where USAXS data have been obtained at small Q, Fig. 2(b) shows that satisfactory fits extend over three decades in Q and seven decades in $d\Sigma/d\Omega$. Over the associated microstructural scale range, Fig. 2(c) shows that the postsinter anneal in air, following vacuum-sintering, has very little effect on the microstructure, as determined by SANS. Table III indicates that the maximum densities attained after air-sintering at 800°C, and vacuum-sintering at 800°C and 850°C were, respectively, 72%, 93%, and 95% TD.

For the three n-ZrO$_2$ sintering studies, Table III presents relevant parameters, derived from the measured sintered densities and SAS model fit results. Figure 6 presents the variations, versus sintering time, of $D_{o\,avg}$ and D_{int}, and Fig. 7, ϕ_{pop} and ϕ_{total}. The variations of S_{pop} and S_v are similar to those of ϕ_{pop} and ϕ_{total}. Results for the as-pressed sample are given in each figure, and the values for the sample, postsinter annealed at 800°C in air for 2 h, are included in Figs. 6(b) and 7(b).

Figure 6 shows that, for all three sintering conditions, the greatest pore coarsening occurs between the as-pressed and

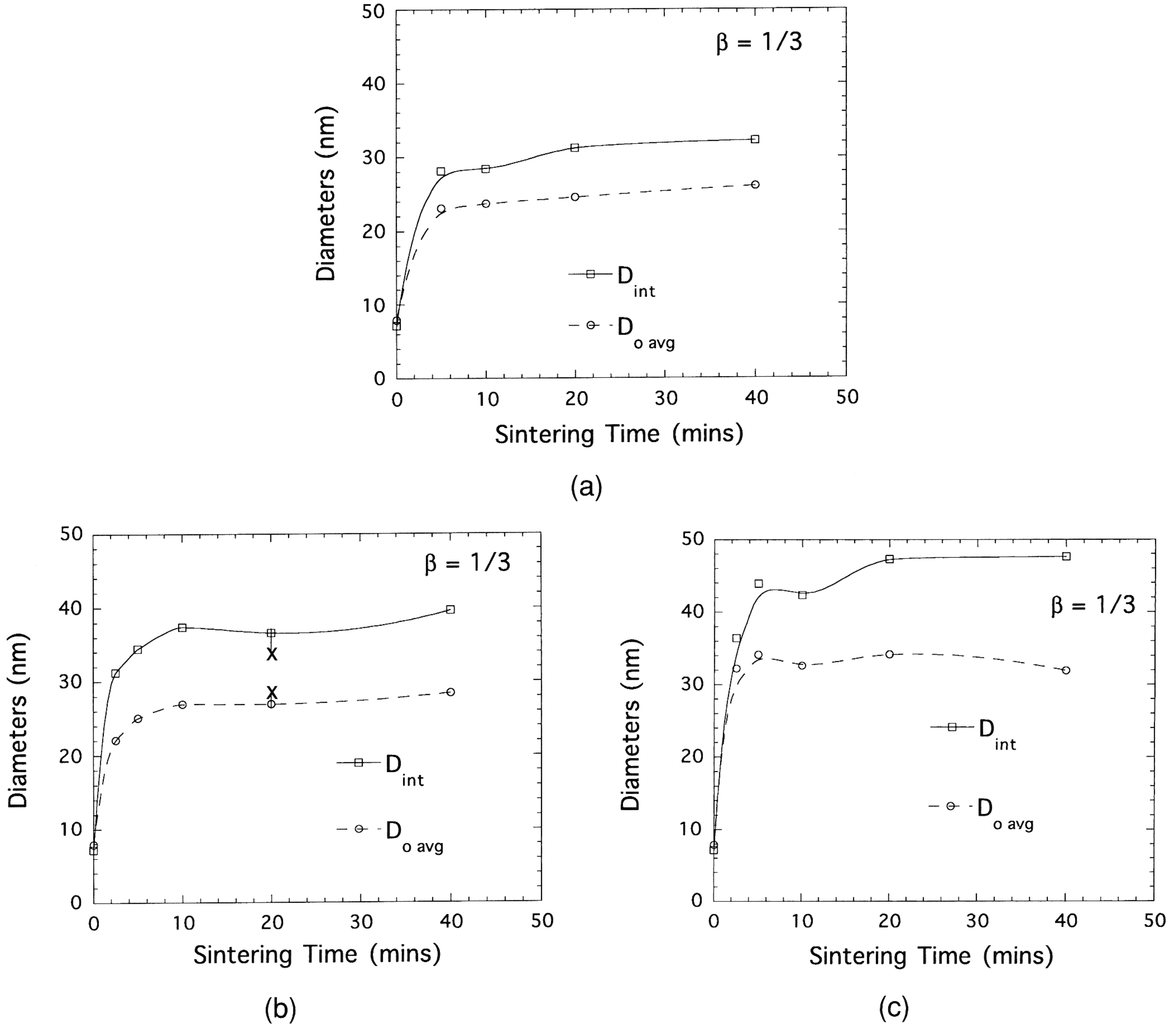

Fig. 6. Evolution during sintering of the SAS model oblate pore population number-weighted mean diameter, $D_{o\ avg}$, and number-weighted mean interpore interference distance, D_{int}, for n-ZrO_2 sintered at (a) 800°C in air, (b) 800°C under vacuum, (c) 850°C under vacuum. In Fig. 6(b), × marks the values for the sample postvacuum-sinter annealed in air.

early sintered states. Thereafter, there is some further coarsening, although, for extended vacuum-sintering at 850°C, there is some evidence of pore shrinkage as full density is approached (decrease in $D_{o\ avg}$, while D_{int} continues to increase). Over the range of partially sintered n-ZrO_2 sample densities studied, the D_{int} diameters are larger than the oblate pore diameters, $D_{o\ avg}$. Given the results for grain and pore diameters from XRD, TEM, SEM and, to some extent, BET, D_{int} appears to be the better SAS microstructural model parameter to associate with the grain diameter, D_{grain}, at least at the higher sintered densities studied. While it is assumed that, at very close to full density, the pore size distribution must shrink and become uncorrelated with the coarsening grain size distribution, the results show that, nevertheless, the former can provide a quantitative assessment of the latter over much of the densification range.

Table III and Fig. 7 show that the SAS model fits account for most of the porosity and surface areas in the partially sintered nanophase samples. This implies that, for a relatively uniform nonagglomerated powder fabrication, consolidation during the early stages of sintering removes most of the coarse pore features and permits the development of a sintered pore/grain microstructure that is largely confined to the nanoscale regime accessible in the SANS measurements. The few coarse features that do remain are well separated in scale from the nanophase microstructure so that the latter is cleanly revealed in the SAS data and can therefore be modeled comprehensively.

Comparison of Figs. 6 and 7 shows that, while greater grain coarsening occurs during vacuum-sintering, higher sintered densities are obtainable at low temperatures. The lower air-sintered densities achieved may be associated with the rapid nanophase sintering rate, which could close the pores sufficiently fast to entrap air within them.[12,13] Despite the reported enhanced diffusion rates, due to the high density of nanophase grain boundaries, the entrapped air may exert sufficient negative sintering pressure to prevent the removal of the residual closed pores. Not only is vacuum-sintering more efficient, but, as Figs. 6(b) and 7(b) show, only minor modifications are introduced into the microstructure during the postsinter annealing in air to restore the ZrO_2 stoichiometry.

Despite the different sintering conditions, the most important variable in determining the nanophase microstructure was found to be the density, where 100% theoretical density (TD) = 5.01×10^3 kg·m^{-3} for cubic n-Y_2O_3 and 5.60×10^3 kg·m^{-3} for monoclinic n-ZrO_2. This does not necessarily imply that each sintering process studied passes through the same intermediate densification stages. However, in Figs. 8–11, dashed lines are

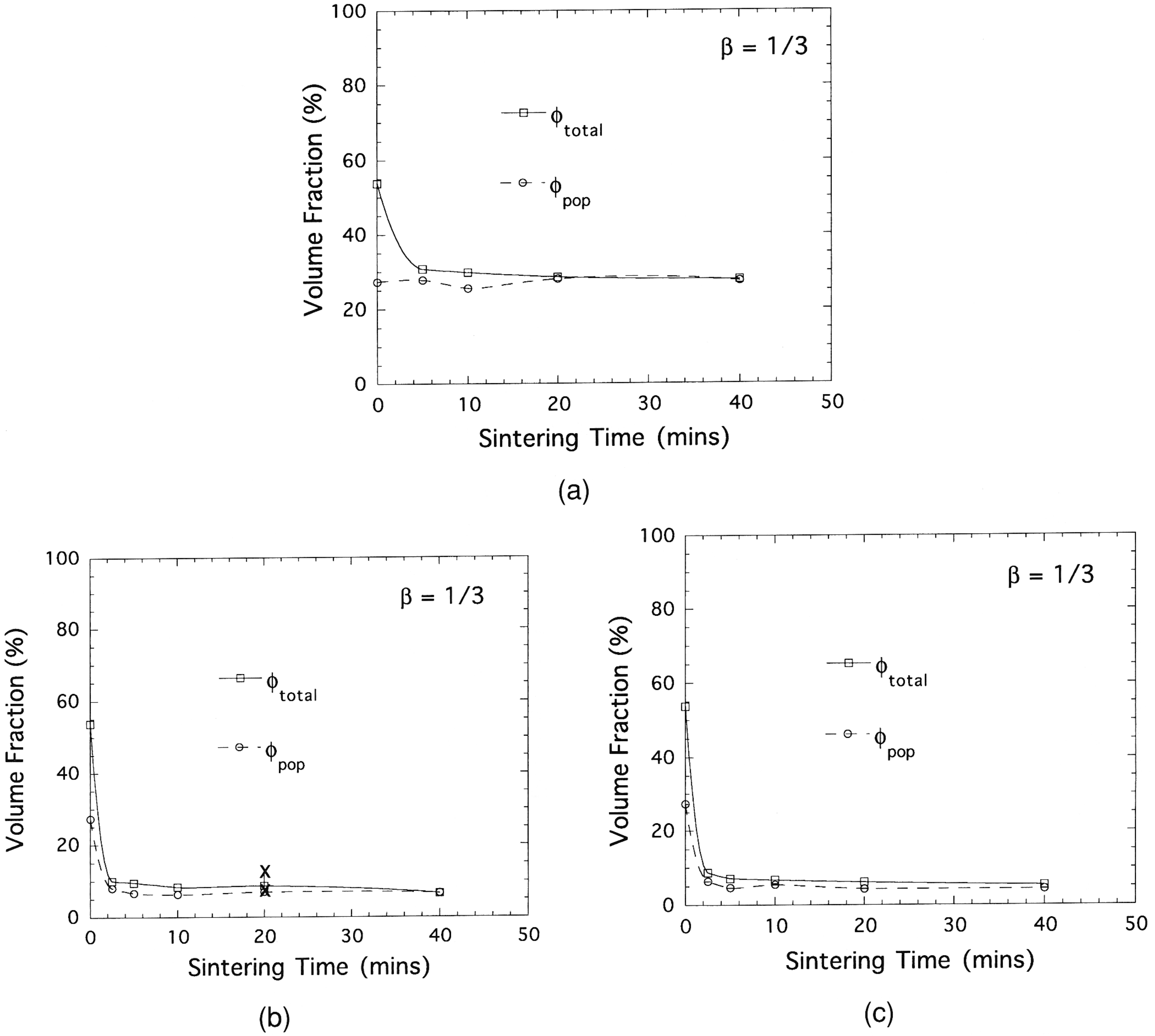

(a)

(b)

(c)

Fig. 7. Evolution during sintering of the SAS model pore population volume fractions, ϕ_{pop}, and total porosities, ϕ_{total} (from density measurements), for (a) 800°C in air, (b) 800°C under vacuum, (c) 850°C under vacuum. In Fig. 7(b), × marks the values for the sample postvacuum-sinter annealed in air.

used to connect the data points for clarity. Figure 8 shows $D_{o\,avg}$ and D_{int} for the three n-ZrO_2 series as a function of density. As with Figs. 9–11, estimated statistical standard uncertainties, σ, given in Table III, are comparable to the symbol sizes. A better measure of sample-to-sample uncertainty is probably given by the scatter in the points. Where measured, means of the XRD and/or TEM/SEM grain diameters are included in Fig. 8. These XRD/TEM/SEM grain diameters are smaller than the corresponding values for D_{int} by 15%–25%, except at the highest densities studied, where D_{int} appears to be in better agreement. $D_{o\,avg}$ is typically some 10%–15% more than the XRD/TEM/SEM values at low densities, but becomes progressively less than these, by as much as 30%, at the highest sintered n-ZrO_2 densities studied. Thus, Fig. 8 supports our earlier view that D_{int} is the more useful overall measure of D_{grain} over much of the n-ZrO_2 density range.

Figure 8 shows the advantage of vacuum-sintering in achieving densities of more than 90% TD, with initial particle coarsening (from 6 nm to 30 nm) comparable with that during air-sintering to only ~70% TD. Extended vacuum-sintering to the highest achievable densities, without the application of compressive forces, was found to cause further coarsening to 40 nm at 800°C, and to 48 nm at 850°C. At even higher sintering temperatures, coarsening became more marked and the nanophase grain size could be lost (as for the n-Y_2O_3 sample sintered at 1200°C, where $D_{o\,avg}$ and D_{int} were both found to exceed 100 nm). Figure 8 suggests that unconstrained vacuum-sintering at temperatures somewhat above 850°C might achieve full density with mean grain diameters ~60 nm. In recent work[23] on vacuum-sintered material, a mean grain size of 75 nm at 97% TD has been achieved.

Figure 9 presents the specific total (Porod) surface areas, S_g, compared with those deduced from the SAS model number-weighted pore size distributions, $S_{g\,pop}$. It shows how most of the surface areas are accounted for in the model and makes clear the enhanced reduction in surface area made possible by vacuum-sintering. Furthermore, the surface area variations appear to follow a single curve, suggesting that intermediate sintering stages may be independent of air- or vacuum-sintering.

Figure 10 presents the percentage widths, ΔW, (relative to $D_{o\,mode}$) of the SAS model number-weighted pore size distribu-

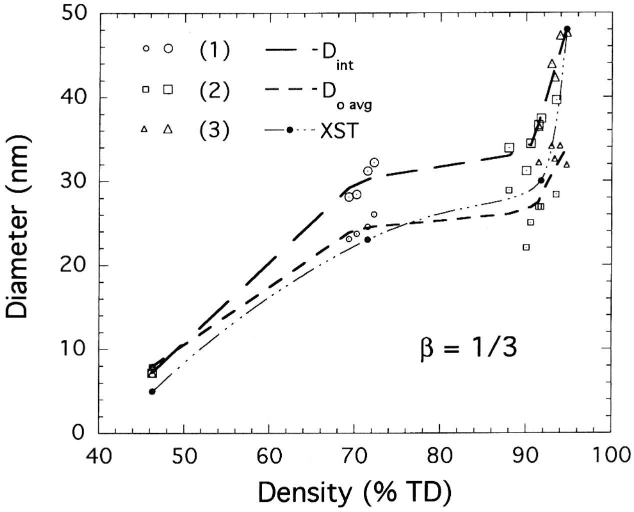

Fig. 8. SAS model pore population interpore interference distance, D_{int} (large symbols), and number-weighted mean diameter, $D_{o\ avg}$ (small symbols), versus density: (1) air-sintered at 800°C, (2) vacuum-sintered at 800°C, and (3) vacuum-sintered at 850°C. The variation in the average of the XRD volume-weighted mean and/or the SEM/TEM number-weighted median grain diameter, denoted XST, is shown for comparison.

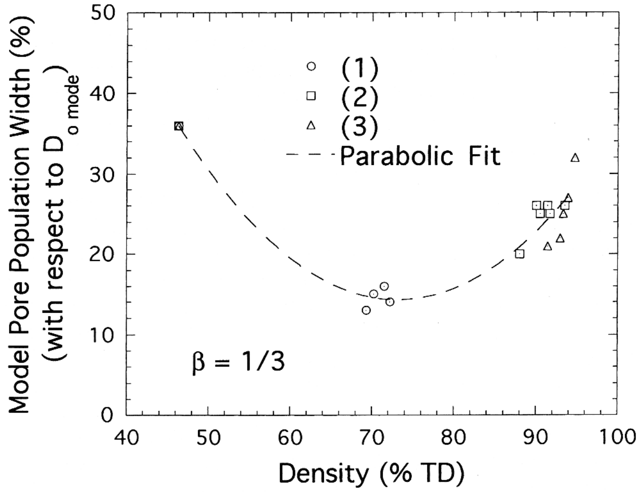

Fig. 10. SAS pore population width, ΔW, versus density for n-ZrO$_2$: (1) air-sintered at 800°C, (2) vacuum-sintered at 800°C, and (3) vacuum-sintered at 850°C.

tions, as a function of sintered density. In the as-pressed condition, ΔW is relatively broad with $\Delta W = 36\%$. For the air-sintered material, $\Delta W = 16\%$, and, for the vacuum-sintered samples, it ranges from $\approx 20\%$ up to $\approx 33\%$ for the densest samples. Thus, the size distribution is narrowest where the interpore interference is strongest, i.e., for intermediate sintered densities (see Fig. 2). This basic result also holds for the n-Y$_2$O$_3$ samples, and may be quite general for the sintering of nanostructured ceramic oxides. Strong SAS interference peaks are an indication of the narrowness of the pore and grain populations, because of the implied uniformity in the interpore distance (D_{int}), which they signify.

A qualitative explanation of Fig. 10 is that, for partially sintered globular particles, the fewest degrees of freedom in the configuration of pores and grains occur close to the dense-random-packed hard-sphere (DRPHS) condition[24] at 64% TD. At lower densities, there are more degrees of freedom, simply because of the lower packing density of the solid grains. At higher densities, there are also more degrees of freedom, because the reduced number of pores permits a greater number of configurations for those that remain around the grains. The broadening in the size distributions, as full density is approached, is in accordance with similar effects observed in the sintering of micrometer-size grain ceramics.[17,25,26] However, multiple components in the pore populations, due to separate processes affecting inter-agglomerate and intra-agglomerate pores,[17] are not observed. This is a further indication of the lack of significant particle agglomeration in the present case.

Figure 11 shows the mean number of oblate pores per nanophase grain in the microstructure, deduced analytically from the SAS model fit parameters and from density measurements. The number of pores has been determined by assuming that the nanostructured porosity, ϕ_{pop}, consists entirely of oblate pores (with orthogonal diameters $D_{o\ avg}$, $D_{o\ avg}$, and $\beta D_{o\ avg}$). The number of grains has been determined by assuming that the solid phase consists of globular grains (mean diameter, $D_{grain} = D_{int}$). While the as-pressed material contains just under one nanophase pore per grain (≈ 0.92), this number is significantly larger, at approximately two pores per grain for all the samples air-sintered at 800°C. The high number density of pores probably enhances the strong interference peak in the SAS data for this series. Break-up of the original pores, as they are closed off

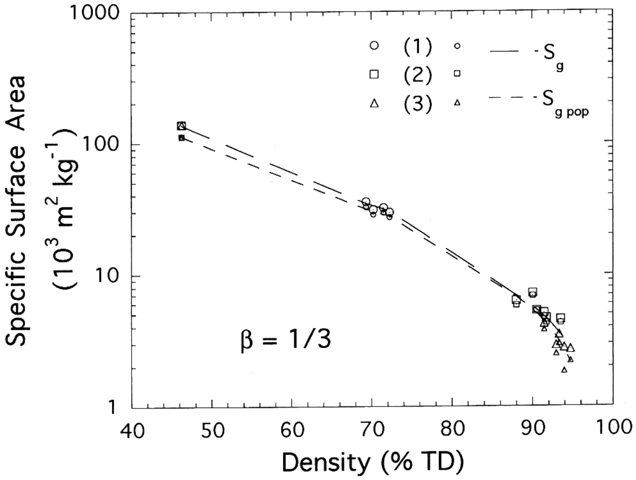

Fig. 9. Total (Porod) specific surface area, S_g (large symbols), and SAS model pore population specific surface area, $S_{g\ pop}$ (small symbols), versus density: (1) air-sintered at 800°C, (2) vacuum-sintered at 800°C, and (3) vacuum-sintered at 850°C.

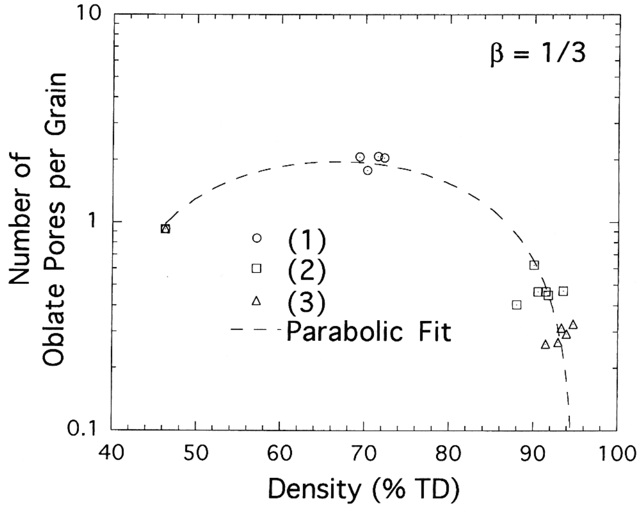

Fig. 11. Deduced number of SAS model oblate pores per nanophase grain versus density for n-ZrO$_2$: (1) air-sintered at 800°C, (2) vacuum-sintered at 800°C, and (3) vacuum-sintered at 850°C.

during the early stages of sintering, is the likely explanation, and the resulting large number of pores per grain is probably associated with the maximum in the pore coordination number expected for the DRPHS condition.[24] For the high-density vacuum-sintered samples, the number of pores per grain is much less, being $\sim$0.45 (falling to $\sim$0.4) for sintering at 800°C, and $\sim$0.3 for sintering at 850°C.

Comparison of $\phi_{\rm pop}$ and $S_{\rm pop}$ indicates that, during air-sintering, the reduction in specific surface area could be largely accounted for by grain coarsening without true sintering. More likely, losses of grain/pore surface area to form sintered grain boundaries are counteracted by surface area gains in more pores per grain. That some of the grain/pore surface area is lost in sintering is independently evidenced by the reduced surface area determined by BET. In vacuum-sintering, grain coarsening cannot account for all of the specific surface area decrease. This and the marked reduction in the number of pores per nanophase grain indicate that much of the surface area loss during vacuum-sintering must be due to the closure of grain boundaries between sintered nanophase particles.[27–29] It is of interest that the vacuum-sintered samples, which, in previous figures, ranked mainly with the density, are clearly separated into the two sintering temperature regimes, when the pore-to-grain ratio is considered. This suggests that, for a given as-pressed starting material, some morphological variations are introduced reproducibly by the sintering thermodynamics, other than those detectable by "conventional" measures of the grain size distributions and sintered densities achieved.

IV. Concluding Discussion

It has been shown how the application of a microstructural model to the SAS data from nanophase ceramics can be used to quantify their microstructural evolution during sintering. The present study suggests that, for the stoichiometry of the n-ZrO$_2$ samples here, vacuum-sintering at a temperature above 850°C could produce fully dense n-ZrO$_2$ with a mean grain diameter of 60 nm. In practice, densities close to full density have been achieved[13,23] at 975°C with grain diameters of 70–80 nm. Furthermore, the model fit results show in detail that the postsinter anneal, to restore full stoichiometry in n-ZrO$_2$ previously vacuum-sintered at 800°C for 20 min, does not significantly affect the final microstructure. Thus, by adjusting the oxygen influx rate during oxidation in the IGC process, and by careful control of the heating rates and sintering temperatures, the stoichiometry can be optimized for sintering without fear of disturbing the microstructure during the postsinter anneal. Further reductions in nanostructured grain diameter are possible (40 nm at near full density) if sinter-forging or hot isostatic pressing (HIP) are combined with a reduced stoichiometry during vacuum-sintering.[23]

To construct reliable and predictive models for the processing conditions, it is essential to determine those parameters that are statistically representative of the undisturbed microstructures present. While TEM- and SEM-based analyses typically sample 100 pores or grains per image, SANS data are representative of $\sim 10^{13}$ pores or grains in a typical partially sintered nanostructured sample. This allows SAS, particularly SANS, to be used with appropriate microstructural models in the evaluation of quantitative and statistically significant parameters that probe the thermodynamics of nanophase ceramic processing.

Acknowledgments: We acknowledge Mr. Michael Roddy for assistance with the electron microscopy studies, and Mr. Rob Woodman for assistance with the nitrogen desorption measurements.

References

[1] R. P. Andes, R. S. Averback, W. L. Brown, L. E. Brus, W. A. Goddard, A. Kaldor, S. G. Louie, M. Moscovits, P. S. Peercy, S. J. Riley, R. W. Siegel, F. Spaepen, and Y. Wang, "Research Opportunities on Clusters and Cluster-Assembled Materials—A Department of Energy Council on Materials Science Panel Report," *J. Mater. Res.*, **4**, 704–36 (1989).

[2] D. L. Bourell, Parimal, and W. Kaysser, "Sol–Gel Synthesis of Nanophase Yttria-Stabilized Tetragonal Zirconia and Densification Behavior below 1600 K," *J. Am. Ceram. Soc.*, **76**, 705–11 (1993).

[3] H. Hahn and R. S. Averback, "The Production of Nanocrystalline Powders by Magnetron Sputtering," *J. Appl. Phys.*, **67**, 1113–15 (1990).

[4] P. G. Sanders, J. R. Weertman, J. G. Barker, and R. W. Siegel, "Small-Angle Neutron Scattering from Nanocrystalline Palladium as a Function of Annealing," *Scr. Metall. Mater.*, **29**, 91–96 (1993).

[5] H. Hahn, J. Logas, and R. S. Averback, "Sintering Characteristics of Nanocrystalline TiO$_2$," *J. Mater. Res.*, **5**, 609–14 (1990).

[6] D. J. Chen and M. J. Mayo, "Densification and Grain Growth of Ultrafine 3 mol % Y$_2$O$_3$–ZrO$_2$ Ceramics," *Nanostruct. Mater.*, **2**, 469–78 (1993).

[7] G. Porod, "General Theory"; Ch. 2, pp. 17–51 in *Small-Angle X-ray Scattering*. Edited by O. Glatter and O. Kratky. Academic Press, London, U.K., 1982.

[8] J. E. Epperson, R. W. Siegel, J. W. White, J. A. Eastman, Y. X. Liao, and A. Narayanasamy, "A Small-Angle Neutron Scattering Investigation of Compacted Nanophase TiO$_2$ and Pd," *Mater. Res. Soc. Symp. Proc.*, **166**, 87–92 (1990).

[9] G. G. Long, P. R. Jemian, J. R. Weertman, D. R. Black, H. E. Burdette, and R. D. Spal, "High-Resolution Small-Angle X-ray Scattering Camera for Anomalous Scattering," *J. Appl. Crystallogr.*, **24**, 30–37 (1991).

[10] X. Zhu, R. Birringer, U. Herr, and H. Gleiter, "X-ray Diffraction Studies of Nanometer-Sized Crystalline Materials," *Phys. Rev. B*, **35**, 9085–90 (1987).

[11] H. P. Klug and L. E. Alexander, "Crystallite Size and Lattice Strains from Line-Broadening"; Ch. 9, pp. 687–90 in *X-ray Diffraction Procedures for Polycrystalline and Amorphous Materials*, 2nd ed. Wiley, San Francisco, CA, 1974.

[12] G. Skandan, C. M. Foster, H. Frase, M. N. Ali, J. C. Parker, and H. Hahn, "Phase Characterization and Stabilization due to Grain Size Effects of Nanostructured Y$_2$O$_3$," *Nanostruct. Mater.*, **1**, 313–18 (1992).

[13] G. Skandan, H. Hahn, M. Roddy, and W. R. Cannon, "Ultrafine-Grained Dense Monoclinic and Tetragonal Zirconia," *J. Am. Ceram. Soc.*, **77**, 1706–10 (1994).

[14] G. Skandan, H. Hahn, and J. C. Parker, "Nanostructured Y$_2$O$_3$: Synthesis and Relation to Microstructure and Properties," *Scr. Metall. Mater.*, **25**, 2389–93 (1991).

[15] G. Skandan, "Processing of Nanostructured Zirconia Ceramics," *Nanostruct. Mater.*, **5**, 111–26 (1995).

[16] S. J. Cregg and K. S. W. Sing, *Surface Area, Adsorption and Porosity*. Academic Press, London, U.K. (1982).

[17] J. M. Wu and C. H. Wu, "Sintering Behavior of Highly Agglomerated Ultrafine Zirconia Powders," *J. Mater. Sci.*, **23**, 3290–99 (1988).

[18] J. S. Pedersen, "Small-Angle Scattering from Precipitates: Analysis by Use of a Polydisperse Hard-Sphere Model," *Phys. Rev. B*, **47**, 657–65 (1993).

[19] P. van Beurten and A. Vrij, "Polydispersity Effects in the Small-Angle Scattering of Concentrated Solutions of Colloidal Spheres," *J. Chem. Phys.*, **74**, 2744–48 (1981).

[20] M. Kotlarchyk and S. H. Chen, "Analysis of Small-Angle Neutron Scattering Spectra from Polydisperse Interacting Colloids," *J. Chem. Phys.*, **79**, 2461–69 (1983).

[21] W. L. Griffith, R. Triolo, and A. L. Compere, "Analytical Scattering Function of a Polydisperse Percus–Yevick Fluid with Schultz- (Γ−) Distributed Diameters," *Phys. Rev. A*, **35**, 2200–206 (1987).

[22] L. C. Roess and C. G. Shull, "X-ray Scattering at Small Angles by Finely-Divided Solids. II. Exact Theory for Random Distributions of Spheroidal Particles," *J. Appl. Phys.*, **18**, 308–13 (1947).

[23] A. J. Allen, S. Krueger, G. G. Long, H. M. Kerch, H. Hahn, and G. Skandan, "Small-Angle Neutron Scattering Studies of Ceramic Nanophase Materials," *Nanostruct. Mater.*, **7**, 113–26 (1996).

[24] J. L. Finney, "Random Packings and the Structure of Simple Liquids: I. The Geometry of Random Close Packing," *Proc. R. Soc. London A*, **319**, 479–93 (1970).

[25] G. G. Long, S. Krueger, and R. A. Page, "The Effect of Green Density and the Role of Magnesium Oxide Additive on the Densification of Alumina Measured by Small-Angle Neutron Scattering," *J. Am. Ceram. Soc.*, **74**, 1578–84 (1991).

[26] S. Krueger, G. G. Long, D. R. Black, D. Minor, P. R. Jemian, G. W. Nieman, and R. A. Page, "Evolution of the Pore Size Distribution in Final-Stage Sintering of Alumina Measured by Small-Angle X-ray Scattering," *J. Am. Ceram. Soc.*, **74**, 2538–46 (1991).

[27] S. Krueger, A. J. Allen, G. G. Long, H. M. Kerch, G. Skandan, and H. Hahn, "Small-Angle Scattering Methods for Characterizing the Sintering of Nanosized Ceramic Powders"; pp. 143–50 in *Proceedings of Joint NIST/NSF Conference on Ultrafine Particle Engineering* (Arlington, VA, May 26–27, 1994). Edited by M. C. Roco, R. D. Shull, and D. T. Shaw. National Science Foundation, Arlington, VA, 1994.

[28] A. J. Allen, G. G. Long, H. M. Kerch, S. Krueger, G. Skandan, H. Hahn, and J. C. Parker, "Sintering Studies of Nanophase Ceramic Oxides Using Small-Angle Scattering," Accepted for publication in *Proceedings of 8th CIMTEC World Ceramics Congress* (Florence, Italy, June 28–July 4, 1994). CIMTEC, Faenza, Italy, 1995.

[29] S. Krueger, A. J. Allen, G. G. Long, H. M. Kerch, G. Skandan, and H. Hahn, "Small-Angle Scattering Methods for Characterizing the Sintering of Nanosized Ceramic Powders"; pp. 359–64 in *Symposium on Neutron Scattering in Materials Science, Proceedings of the Materials Research Society Symposium (Boston, MA, November, 1994, MRS Proc.* **376**). Edited by D. A. Newman, T. P. Russell, and B. J. Wuensch. Materials Research Society, Pittsburgh, PA, 1995. □